Tunable magnetic anisotropy in multiferroic oxides

Xue-Zeng Lu and James M. Rondinelli [*]

Department of Materials Science and Engineering, Northwestern University, Evanston, Illinois 60208, USA

Room-temperature electric-field control of magnetism is actively sought to realize electric-field assisted changes in perpendicular magnetic anisotropy (PMA), which is important to magnetic random access memories (MRAMs) and future spin-orbit based logic technologies. Traditional routes to achieve such control rely on heterostructures of ferromagnets and/or ferroelectrics, exploiting interfacial effects, including strain generated by the substrate, or electric-field induced changes in the interfacial electronic structures. Here we present design rules based on d-orbital splitting in an octahedral field and crystallographic symmetries for electric-field control of PMA utilizing hybrid improper ferroelectricity by scaffolding simple perovskite oxides into ultrashort period superlattices, $(ABO_3)_1/(A'BO_3)_1$, and in multiferroic $AA'BB'O_6$ double perovskites. We validate the strategy using first principles calculations and a single-ion anisotropic model. We find a change in the magnetic anisotropy from the *in-plane* to the *out of plane* direction in $(BiFeO_3)_1/(LaFeO_3)_1$ and a 50% decrease of the magnetization along the out of plane direction in $LaYNiMnO_6$, when a polar to nonpolar phase transition occurs with strain. The origin of the PMA control is due to the structural tunable competitions among the t_{2g} and e_g orbital interactions on the magnetic ions arising from relativistic spin-orbital interactions that are susceptible to changes in the oxygen octahedral tilts across the field-tunable transition. Our results allow us to search rapidly for other promising multiferroics materials with voltage-controlled magnetic anisotropy for applications in low-energy information storage and logic devices.

I. INTRODUCTION

Electric-field controllable magnetism (EFCM) offers a route towards low-energy information storage and new forms of logic devices [1,2]. Several strategies were reported in ferromagnetic films or semiconductors [3–6], magneto-electric multiferroics [7–9], heterostructures or superlattices consisting of ferromagnets and/or ferroelectrics [10–17], multidomain and domain wall structures [18–26], perovskite thin films [27–29], and hybrid improper ferroelectrics [30–33]. The aspirational goal of these materials platforms is to realize tunable perpendicular magnetic anisotropy (PMA) [34,35], with most realizations of electric-field assisted changes in PMA occurring in ferromagnetic films on semiconductors [3–6] or in ferromagnetic and/or ferroelectric heterostructures [12–15,34]. Materials and mechanisms to realize electric-field controllable PMA in multiferroics with large ferroelectricity (e.g., $> 1\,C/m^2$) and strong ferromagnetism (e.g., $> 1\mu_B$ per transition metal ion) at room temperature, however, remains a challenge [35], despite experimentally demonstrated electric-field control of *in-plane* magnetic anisotropy in $BiFeO_3$ [19,20,22] and predicted control in $LiNbO_3$-type Zn_2FeOsO_6 [36] and double perovskite $LaSrMnOsO_6$ [37]. From a processing perspective, it is desirable to realize PMA control from single phase multiferroic materials rather than requiring complex multicomponent heterostructures.

In 2011, Benedek and Fennie proposed that hybrid improper ferroelectricity (HIF) is active in Ruddlesden-Popper $Ca_3B_2O_7$ ($B = $ Mn, Ti) materials [31], which was experimentally demonstrated later [38–41]. In these compounds, the polar mode ($Q_{\Gamma_5^-}$), and oxygen octahedral *rotation* (OOR) ($Q_{X_2^+}$), and oxygen octahedral *tilt* (OOT) ($Q_{X_3^-}$) modes couple through a trilinear interaction, $Q_{\Gamma_5^-}Q_{X_2^+}Q_{X_3^-}$, to stabilize the polar ground state structure with $Cmc2_1$ symmetry. The functional electric polarization P is proportional to $Q_{X_2^+}Q_{X_3^-}$ owing to the HIF mechanism. Moreover, the direction of weak ferromagnetism (wFM), which is due to the antisymmetric Dzyaloshinskii-Moriya (DM) exchange interaction, is controlled by the tilt $Q_{X_3^-}$ mode (OOT) that occurs about the short crystallographic axes in the magnetic members of this family. Here, the direction of the wFM can be switched by an in-plane electric field through coupling to the polarization, which in turn reverses the $Q_{X_3^-}$ mode. Later, the HIF mechanism was extended to 1/1 period A-site cation ordered perovskite superlattices [33], which led to the theoretical prediction of ultrashort period $BiFeO_3/LaFeO_3$ superlattices exhibiting room-temperature EFCM [42]. To the best of our knowledge, reported EFCM mechanisms rely on the aforementioned DM induced wFM controlled by the OOT mode [30]. The tunable wFM induced by the DM interactions is also key to other promising candidates for the EFCM in multiferroics at room temperature [43,44]. Remarkably, there are no assessments concerning the viability of electric-field tunable *magnetic anisotropy* in HIF materials despite the potential of HIF to serve as a unique mechanism from which to design multiferroics exhibiting simultaneously large ferroelectricity, strong ferromagnetism, and strong magnetoelectricity.

Here, we propose design rules to tune the magnetic anisotropy, which may be used to explore electric-field control of perpendicular magnetic anisotropy, utilizing a combination

---

[*]jrondinelli@northwestern.edu
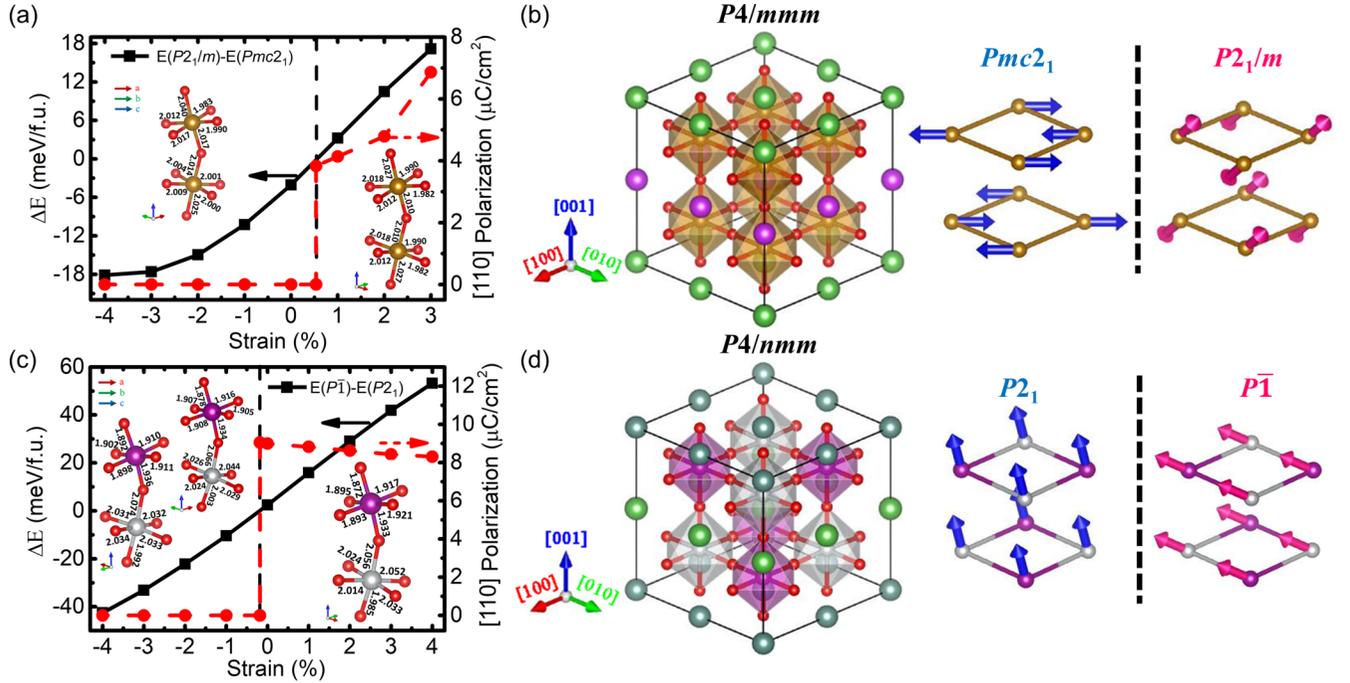
FIG. 1. (a) Computed energies (left axis) and polarizations (right axis) with respect to the biaxial strain for $BiFeO_3/LaFeO_3$. The energy difference is between $P2_1/m$ and $Pmc2_1$. (b) The magnetic anisotropies in the $Pmc2_1$ and $P2_1/m$ phases. High symmetry $P4/mmm$ structure of $BiFeO_3/LaFeO_3$ is also shown on the left. The blue and pink arrows indicate the spin directions in the $Pmc2_1$ and $P2_1/m$ phases, respectively. Only the iron sublattice is shown for clarity. (c) Energies (left axis) and polarizations (right axis) with respect to the biaxial strain for $LaYNiMnO_6$. The energy difference is between $P\bar{1}$ and $P2_1$. (d) The magnetic anisotropies in the $P2_1$ and $P\bar{1}$ phases. High symmetry $P4/nmm$ structure of $LaYNiMnO_6$ is also shown on the left. The blue and pink arrows indicate the spin directions in the $P2_1$ and $P\bar{1}$ phases, respectively. Only the manganese and nickel sublattice is shown. Insets in (a), (c) show the comparison of the Fe-site coordination between the $Pmc2_1$ (right) and $P2_1/m$ (left) phases and comparison of Mn- and Ni-site coordinations for the $P2_1$ (right) and $P\bar{1}$ (left) phases, respectively. Bond lengths are in units of Å. The crystallographic axes are shown for the local environment.

of density functional theory (DFT) calculations and single-ion anisotropic models, in $(ABO_3)_1/(A'BO_3)_1$ superlattices and $AA'BB'O_6$ double perovskites exhibiting HIF. We first show a change of the magnetic anisotropy from an in-plane to out of plane direction in experimentally synthesizable $BiFeO_3/LaFeO_3$ superlattices across a polar to nonpolar (P to NP) phase transition that may be induced by applying electric field. Next, we find a 50% decrease of the magnetization along the out of plane direction in double perovskite $LaYNiMnO_6$ across an analogous P to NP phase transition. The tunable magnetic anisotropy is due to the changes in the oxide ligand fields about the magnetic ions induced by changes in the character of the oxygen octahedral tilts across the transition. This tilt-anisotropy sensitivity arises from the spin-orbital interactions (SOIs) among the t_{2g} and e_g orbitals on the magnetic ions, which can either produce *easy-plane* or *easy-axis* anisotropies, because SOIs are controlled by the oxygen octahedral tilt symmetry. From this understanding, we formulate two design principles for ferroelectric control of the magnetic anisotropy: (1) orbital splitting criterion: selecting d^n magnetic ions with the highest occupied or lowest unoccupied orbitals of xy symmetry to be nearly degenerate with at least one of the other two t_{2g} orbitals (such as Mn^{4+} with d^3 and Fe^{3+} d^5 configurations); and (2) polymorphism criterion: a ferroelectric phase with a low-energy metastable state exhibiting either an abrupt change in magnitude or distinct change in pattern of the oxygen octahedral tilts (such as in the

P to NP transition). Our study calls for careful examination of the magnetic anisotropy changes that occur along with structural phase transitions in other multiferroics materials.

II. TUNABLE MAGNETIC ANISOTROPY

A. Polar to nonpolar phase transitions in 1:1 $BiFeO_3/LaFeO_3$ superlattice

We showed previously that the P to NP transition is a general feature in $(ABO_3)_1/(A'BO_3)_1$ superlattices and $AA'BB'O_6$ double perovskites exhibiting HIF [45], because the hidden nonpolar phase originates from the competition between the anharmonic (trilinear) octahedral derived mode interactions that stabilize HIF in the polar phase and hybrid improper antiferroelectricity in the nonpolar phase. Figure 1(a) shows a similar P to NP ($Pmc2_1$ to $P2_1/m$ symmetry) transition occurs at ≈0.5% strain in the $BiFeO_3/LaFeO_3$ superlattice, and that tensile strain favors the polar $Pmc2_1$ phase whereas compressive strain favors the nonpolar $P2_1/m$ phase. This ferrate strain phase diagram is consistent with other $(ABO_3)_1/(A'BO_3)_1$ superlattices [45]. At the $Pmc2_1$ to $P2_1/m$ transition there is a sudden decrease in electric polarization from $4\,\mu C/cm^2$ to zero at 0.5% strain. Because of the trilinear couplings among P, OOT, and OOR modes in $Pmc2_1$, the transition also changes the character of the OOT and OOR modes. The OOT mode along [110] transforms into two unique and independent OOTs along

[100] and along [010], while the OORs become out of phase in the $P2_1/m$ phase [see inset of Fig. 1(a) and details below]. The corresponding changes in the magnitudes of the OOT and OOR modes are very small. Although previous reports showed the polar $Pmc2_1$ phase remains stable at -1% strain (corresponding to -1.1% in our definition) [42], this quantitative value for the critical strain may be due to the different exchange-correlation functional used. Reference [42] uses the local spin density approximation with the plus Hubbard U correction (LSDA+U) whereas we use the revised Perdew-Burke-Ernzerhof functional for solids with the plus U method (PBEsol+U) following Ref. [44] (see also Refs. [45–48] therein). The existence of the nonpolar $P2_1/m$ phase under strain is also supported by our Landau model and genetic algorithm (GA) structural search method [49,50].

B. Model analysis of the tunable magnetic anisotropy across the P to NP transition

Next we perform DFT+U+SOC (spin-orbital coupling) calculations and find that the in-plane magnetic anisotropy in the $Pmc2_1$ phase of the G-type antiferromagnetic (AFM) BiFeO$_3$/LaFeO$_3$ superlattice is along the [1$\bar{1}$0] direction, which is perpendicular to the [110] electric polarization direction. This result is consistent with that in Ref. [42]. Interestingly, our calculations for the $P2_1/m$ phase indicate that the magnetic anisotropy is along the [011] direction [Fig. 1(b)]. Thus, we expect that an in-plane electric field ($\boldsymbol{E}$) may control the magnetic anisotropy across a $Pmc2_1$ to $P2_1/m$ (P to NP) transition through its coupling to the polarization ($\boldsymbol{P}$) through the term $\propto \boldsymbol{P} \cdot \boldsymbol{E}$ in the free energy describing the compound.

To further elucidate the origins of the different magnetic anisotropies in the two phases, we next employ a phenomenological model with the spin Hamiltonian expressed as [51,52]

$$\hat{H}_{\text{spin}} = \sum_{i<j} J_{ij}\vec{S}_i \cdot \vec{S}_j + \sum_{i<j} \vec{D}_{ij} \cdot (\vec{S}_i \times \vec{S}_j) + \sum_{i,\alpha\beta} A_{i,\alpha\beta}\vec{S}_{i\alpha}\vec{S}_{i\beta},$$

(1)

where J_{ij} and $\vec{D}_{ij}$ are the symmetric spin exchange and antisymmetric DM exchange interaction parameters, respectively, between magnetic ions i with spin $\vec{S}_i$ and j with $\vec{S}_j$. $A_{i,\alpha\beta}$ is the single-ion anisotropy parameter of ion i ($\alpha, \beta = x, y, z$). Although the DM exchange interaction induces spin canting and may affect the magnetic anisotropy direction [36], single-ion anisotropy (SIA) usually governs the principal spin direction. In addition, the spin canting angle is usually very small, for example, $0.7°$ in BiFeO$_3$/LaFeO$_3$ with a calculated wFM of $\approx 0.05\,\mu_B$/Fe and a remanent moment of $4\,\mu_B$/Fe [42]. Therefore, we focus on changes in the SIA term across the P to NP transition on the magnetic anisotropy, which we express as

$$\hat{H}_{\text{SIA}} = A_{i,xx}S_x^2 + A_{i,yy}S_y^2 + A_{i,zz}S_z^2 + 2A_{i,xy}S_xS_y$$
$$+ 2A_{i,xz}S_xS_z + 2A_{i,yz}S_yS_z$$
$$= A_{i,xx}|\vec{S}|^2 + (A_{i,yy} - A_{i,xx})S_y^2 + (A_{i,zz} - A_{i,xx})S_z^2$$
$$+ 2A_{i,xy}S_xS_y + 2A_{i,xz}S_xS_z + 2A_{i,yz}S_yS_z.$$

(2)

The effects of the DM exchange interaction on the magnetic anisotropy can be found in the Supplemental Material [53] (see also Refs. [54,55] therein).

We then compute the effective parameters $A_{i,yy} - A_{i,xx}$, $A_{i,zz} - A_{i,xx}$, $A_{i,xy}$, $A_{i,xz}$, and $A_{i,yz}$ using a four-states mapping method with our DFT+U+SOC calculations with $|\vec{S}| = 1$ for each phase at 0% strain. Next, we minimize $\hat{H}_{\text{SIA}}$ to obtain the SIA direction $\vec{S} = (\sin\theta\cos\varphi, \sin\theta\sin\varphi, \cos\theta)$ given by the polar (θ) and azimuthal (φ) angles as described in Ref. [53] (see also Ref. [56] therein). We find that the SIA on the single symmetry unique iron site in the $Pmc2_1$ phase is close to the in-plane [1$\bar{1}$0] direction ($\vec{S} = 0.62, -0.70, -0.36$). In contrast, there are two symmetry inequivalent Fe sites in the nonpolar $P2_1/m$ phase with the SIA very close to the [010] and [001] directions (Figs. S2 and S3 in the Supplemental Mayerial [53]), respectively, $\vec{S}_1 = (-0.09, 0.94, 0.34)$ and $\vec{S}_2 = (-0.19, -0.30, -0.94)$. For each phase, we next minimize the sum of $\hat{H}_{\text{SIA}}$ over all iron sites in the unit cell to obtain the magnetic anisotropy, which agrees with our direct DFT+U+SOC calculations [Fig. 1(b)]. Therefore, we conclude here that the change in magnetic anisotropy across the P to NP transition originates from the dramatically different SIA on the iron sites, which the oxygen sublattice geometry imparts, i.e., the rotations, tilts, and other secondary distortions.

C. Effects of the phonon modes on the magnetic anisotropy

Displacive atomic distortions are known to affect SIA in magnetic materials [57,58]. Therefore, we next decompose the atomic displacements that produce the $Pmc2_1$ and $P2_1/m$ structures from the ideal $P4/mmm$ high symmetry structure into symmetry-adapted normal modes (Fig. 2) to assess each mode's contribution to the SIA. In the polar $Pmc2_1$ phase, there are three important modes: an in-plane ferroelectric (FE) mode along [110] transforming as the irreducible representation (irrep) Γ_5^-, an oxygen octahedral rotation (OOR) mode about [001] (M_2^+), and an oxygen octahedral tilt (OOT) about [110] (M_5^-). For the nonpolar $P2_1/m$ structure there are two in-plane antiferroelectric (AFE) modes along [100] (Γ_5^+ and X_3^-), two AFE modes along [001] (M_3^- and X_2^-), an OOR about [001] (M_4^-), and two OOTs about [100] and [010] (M_5^- and X_1^+). One key difference between the two phases is the decoupled [100] and [010] OOTs in $P2_1/m$, which will be important to achieve control of the magnetic anisotropy upon the phase transition.

By computing the SIA in a hypothetical structure, obtained from adding each mode with an amplitude given by the equilibrium phases at 0% strain into the $P4/mmm$ structure, we obtain that mode's contribution to the SIA (Fig. 3). For the polar $Pmc2_1$ structure, both the Γ_5^- FE and M_2^+ OOR modes favor SIA close to the film normal direction, whereas the M_5^- OOT mode favors SIA close to the in-plane [1$\bar{1}$0] direction. Thus, the OOT mode dominates among the SIA contributions to give the overall in-plane [1$\bar{1}$0] magnetic anisotropy in the polar phase [Fig. 1(b)]. For the nonpolar $P2_1/m$ phase, we find the mode dependent SIA is more complex, because there are more distortions and more sites to consider: the Γ_5^+ AFE mode favors SIA close to the [100] direction, the M_3^- AFE
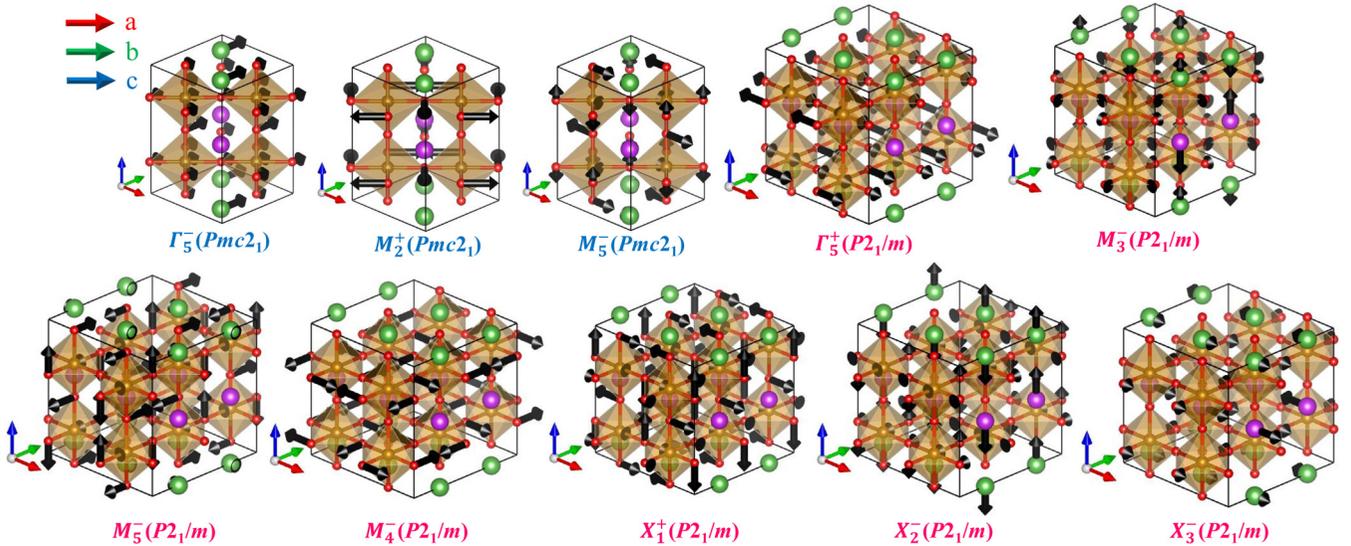
FIG. 2. The modes in the $Pmc2_1$ and $P2_1/m$ structures are obtained by decomposing the ion displacements in each structure with respect to $P4/mmm$ of BiFeO$_3$/LaFeO$_3$. Mode naming conventions can be found in section C of the main text. The black arrows indicate the direction and magnitude of the ion displacements.

mode favors SIA in the (001) plane and is close to the [010] direction, the M_4^- OOR mode favors out of plane SIA, the M_5^- OOT mode favors in-plane [010] SIA, the X_1^+ OOT mode favors in-plane [100] SIA, the X_2^- AFE mode favors SIA

in the (010) plane and close to the [100] direction, and the X_3^- AFE mode favors SIA close to the [100] direction. We find that the values for the SIA parameters given by the Γ_5^+ and M_3^- AFE modes are small compared with other modes
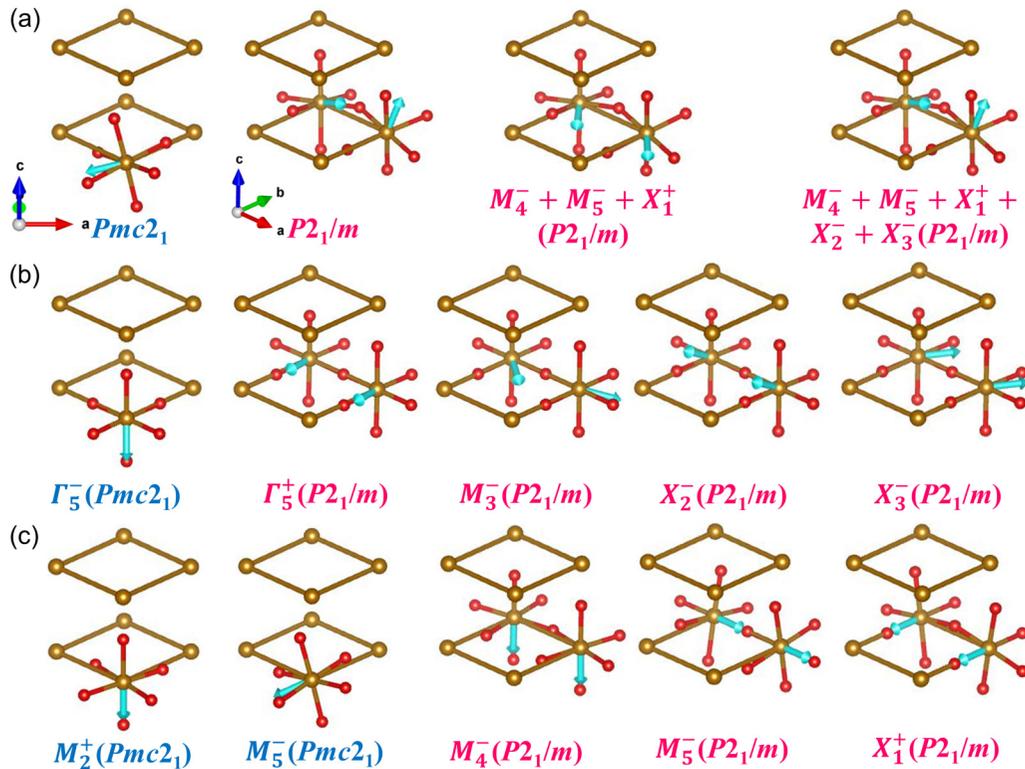
FIG. 3. The single-ion anisotropy (SIA) obtained in BiFeO$_3$/LaFeO$_3$ with (a) multiple modes, (b) single (anti-)ferroelectric mode, and (c) single oxygen octahedral modes included in the $P4/mmm$ structure. Each mode is represented by its irrep and corresponding phase. $Pmc2_1$ and $P2_1/m$ indicate that all the correlated modes leading to the specified symmetries are included. The light blue arrow indicates the direction of the single-ion anisotropy and only the iron sublattice and the local octahedron are shown for clarity. The crystallographic axes are shown for the two phases.
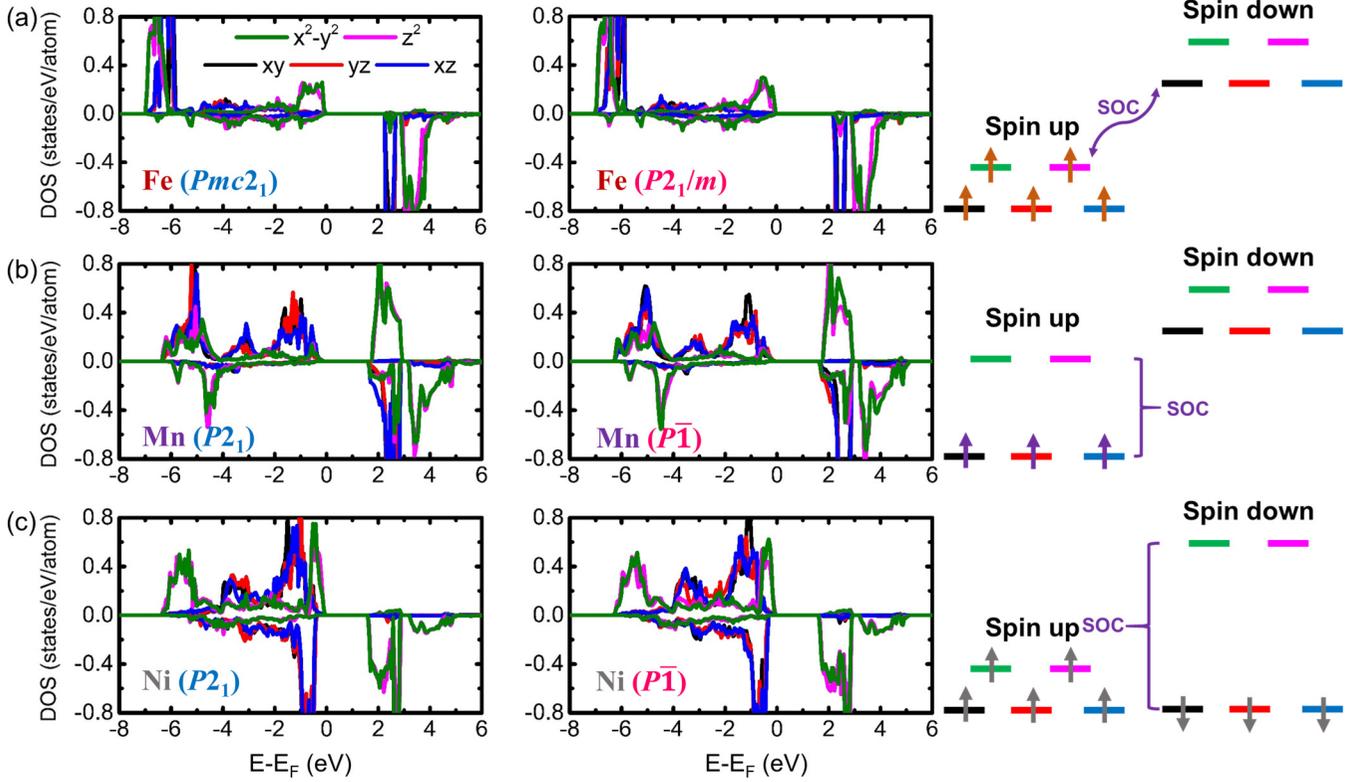
FIG. 4. (a) Orbital projected iron atom density of states (DOS) in $Pmc2_1$ and $P2_1/m$ and the schematic illustration of the orbital configuration in $BiFeO_3/LaFeO_3$. (b), (c) show the density of states of manganese and nickel atoms in $P2_1$ and $P\bar{1}$ and the schematic illustration of the corresponding orbital configurations in $LaYNiMnO_6$. There are two symmetry inequivalent iron atom sites in $P2_1/m$ and two symmetry inequivalent manganese and nickels, respectively, in $P\bar{1}$ and the density of states for the other iron atom in $P2_1/m$, and manganese and nickel atoms in $P\bar{1}$ are shown in the Supplemental Material. SOC is not included in these calculations.

active in the $P2_1/m$ phase, suggesting that their effects on the SIA can be neglected [Fig. 3(a)]. Furthermore, the OOR (M_4^-) and OOT (M_5^- and X_1^+) modes also lead to in-plane SIA, but close to the [110] direction, which indicates that the OOT modes also dominate the contributions from the OOR mode in the $P2_1/m$ phase—similar to our finding in the polar $Pmc2_1$ structure. The final magnetic anisotropy in the $P2_1/m$ phase must include contributions from the X_2^- and X_3^- AFE modes [Fig. 3(a)]. Because the OOR and OOT modes in both phases are primary modes [49], this mode- and site-resolved SIA assessment allows us to conclude that the decoupling of the OOT modes across the polar to nonpolar transition ($M_5^- \rightarrow M_5^- + X_1^+$) sufficiently alters the Fe^{3+} coordination environments [inset of Fig. 1(a)] so as to trigger a net change in the SIA direction from one phase to another.

D. Origin of the tunable magnetic anisotropy across the polar to nonpolar transition

The physical origin of SIA can be ascribed to SOC effects (i.e., $\lambda \hat{\boldsymbol{L}} \cdot \hat{\boldsymbol{S}}$) in perturbation theory [52,59], where $\lambda > 0$ if the orbital filling from unpaired electrons is less than half full for that manifold and $\lambda < 0$ otherwise. The $\lambda \hat{\boldsymbol{L}} \cdot \hat{\boldsymbol{S}}$ term can be further expanded as

$$
\begin{aligned}
\lambda \hat{\boldsymbol{L}} \cdot \hat{\boldsymbol{S}} = {} & \lambda \hat{S}_{z'} \left(\hat{L}_z \cos\theta + \frac{1}{2}\hat{L}_+ e^{-i\varphi}\sin\theta + \frac{1}{2}\hat{L}_- e^{i\varphi}\sin\theta \right) \\
& + \frac{\lambda}{2}\hat{S}_{+'}\left(-\hat{L}_z \sin\theta - \hat{L}_+ e^{-i\varphi}\sin^2\frac{\theta}{2} + \hat{L}_- e^{i\varphi}\cos^2\frac{\theta}{2} \right) \\
& + \frac{\lambda}{2}\hat{S}_{-'}\left(-\hat{L}_z \sin\theta + \hat{L}_+ e^{-i\varphi}\cos^2\frac{\theta}{2} - \hat{L}_- e^{i\varphi}\sin^2\frac{\theta}{2} \right),
\end{aligned}
\tag{3}
$$

where the orbital angular momentum operator $\hat{\boldsymbol{L}}$ and spin angular momentum operator $\hat{\boldsymbol{S}}$ are in (x, y, z) and (x', y', z') Cartesian coordinates, respectively. θ and φ are the polar and azimuthal angles, respectively, of the spin direction (i.e., z' direction) with respect to the (x, y, z) coordinates. $\hat{L}_+ = \hat{L}_x + i\hat{L}_y$ and $\hat{L}_- = \hat{L}_x - i\hat{L}_y$ are ladder operators, and $\hat{S}_+$ and $\hat{S}_-$ are specified in the same manner as $\hat{L}_+$ and $\hat{L}_-$, respectively. As shown from the electronic density of states (DOS) in Fig. 4(a) (additional details can be found in the Supplemental Material [53]), the Fe^{3+} d^5 orbital configurations in the two phases are similar and the energetic ordering and filling of the orbitals are approximately described as $(|xy\uparrow\rangle, |xz\uparrow\rangle, |yz\uparrow\rangle)^1 < (|x^2-y^2\uparrow\rangle, |z^2\uparrow\rangle)^1 < (|xy\downarrow\rangle, |xz\downarrow\rangle, |yz\downarrow\rangle)^0 < (|x^2-y^2\downarrow\rangle, |z^2\downarrow\rangle)^0$, where $\uparrow$ and $\downarrow$

TABLE I. Values of (θ, φ) computed by minimizing $-|\langle i|\lambda\hat{L}\cdot\hat{S}|j\rangle|^2$, where $i, j = |xy\rangle, |xz\rangle, |yz\rangle, |x^2-y^2\rangle$, or $|z^2\rangle$. The definition of (θ, φ) is shown in the main text and "–" indicates the values are not available.

	$|xy\rangle$	$|xz\rangle$	$|yz\rangle$	$|x^2-y^2\rangle$	$|z^2\rangle$
$\lambda\hat{L}\cdot\hat{S} = \hat{H}^0_{SO}$ for SOC between spins with same directions					
$\langle xy|$	–	$(\frac{\pi}{2},0)$	$(\frac{\pi}{2},\frac{\pi}{2})$	$(0,-)$	–
$\langle xz|$	$(\frac{\pi}{2},0)$	–	$(0,-)$	$(\frac{\pi}{2},\frac{\pi}{2})$	$(\frac{\pi}{2},\frac{\pi}{2})$
$\langle yz|$	$(\frac{\pi}{2},\frac{\pi}{2})$	$(0,-)$	–	$(\frac{\pi}{2},0)$	$(\frac{\pi}{2},0)$
$\langle x^2-y^2|$	$(0,-)$	$(\frac{\pi}{2},\frac{\pi}{2})$	$(\frac{\pi}{2},0)$	–	–
$\langle z^2|$	–	$(\frac{\pi}{2},\frac{\pi}{2})$	$(\frac{\pi}{2},0)$	–	–
$\lambda\hat{L}\cdot\hat{S} = \hat{H}'_{SO}$ for SOC between spins with opposite directions					
$\langle xy|$	–	$(-,\frac{\pi}{2})$	$(-,0)$	$(\frac{\pi}{2},-)$	–
$\langle xz|$	$(-,\frac{\pi}{2})$	–	$(\frac{\pi}{2},-)$	$(-,0)$	$(-,0)$
$\langle yz|$	$(-,0)$	$(\frac{\pi}{2},-)$	–	$(-,\frac{\pi}{2})$	$(-,\frac{\pi}{2})$
$\langle x^2-y^2|$	$(\frac{\pi}{2},-)$	$(-,0)$	$(-,\frac{\pi}{2})$	–	–
$\langle z^2|$	–	$(-,0)$	$(-,\frac{\pi}{2})$	–	–

represent spin up and spin down states, respectively. It should be noted that none of the orbitals are energetically degenerate owing to the reduced C_{2v} and C_{2h} Fe-site symmetries, respectively, in the $Pmc2_1$ and $P2_1/m$ structures.

We focus on the SOC interactions between the $(|x^2-y^2\uparrow\rangle, |z^2\uparrow\rangle)^1$ and $(|xy\rangle, |xz\downarrow\rangle, |yz\downarrow\rangle)^0$ states that occur due to the spin-nonconserving terms, $\hat{H}'_{SO} = \frac{\lambda}{2}\hat{S}_{+'}(-\hat{L}_z\sin\theta - \hat{L}_+e^{-i\varphi}\sin^2\frac{\theta}{2} + \hat{L}_-e^{i\varphi}\cos^2\frac{\theta}{2}) + \frac{\lambda}{2}\hat{S}_{-'}(-\hat{L}_z\sin\theta + \hat{L}_+e^{-i\varphi}\cos^2\frac{\theta}{2} - \hat{L}_-e^{i\varphi}\sin^2\frac{\theta}{2})$, with an energy gain from matrix elements of the form $-\frac{|\langle i|\hat{H}'_{SO}|j\rangle|^2}{|e_i - e_j|}$ where $i = |x^2-y^2\uparrow\rangle, |z^2\uparrow\rangle$ and $j = |xy\downarrow\rangle, |xz\downarrow\rangle, |yz\downarrow\rangle$ and e_i and e_j represent the corresponding orbital energies. These spin-orbit interactions occur between only occupied and unoccupied orbitals and those terms with small energy differences (i.e., $|e_i - e_j|$) significantly contribute to the SIA energy determining the spin direction. As can be seen in Table I, $|x^2-y^2\uparrow\rangle$ can interact with $|xy\downarrow\rangle$ through $\hat{L}_z$, leading to an in-plane SIA; $|x^2-y^2\uparrow\rangle/|z^2\uparrow\rangle$ can interact with $|xz\downarrow\rangle$ through $\hat{L}_+/\hat{L}_-$, leading to SIA in the (010) plane; and $|x^2-y^2\uparrow\rangle/|z^2\uparrow\rangle$ can interact with $|yz\downarrow\rangle$ through $\hat{L}_+/\hat{L}_-$, leading to the SIA in the (100) plane.

The competitions among pairwise orbital interactions $|x^2-y^2\uparrow\rangle$ and $|xy\downarrow\rangle$, $|x^2-y^2\uparrow\rangle/|z^2\uparrow\rangle$, and $|xz\downarrow\rangle/|yz\downarrow\rangle$ will be sensitive to any perturbations to the ligand-imposed crystal field about the Fe site, because the nominal e_g symmetry orbitals $|x^2-y^2\uparrow\rangle$, $|z^2\uparrow\rangle$ and the t_{2g} orbitals $|xy\downarrow\rangle$, $|xz\downarrow\rangle$, $|yz\downarrow\rangle$ are nearly degenerate, respectively. We then expect macroscopically different SIA directions due to the different displacive modes (see Fig. 3). For this reason, SIA arising from such competitions can be tuned through a structural phase transition, manifesting as changes to the active modes that describe the equilibrium structures on either side of the transition. Even in the same structure, if the symmetry environments of the magnetic ions are different, the SIA should be considerably different for those sites, such as those in the $P2_1/m$ phase. Therefore, we attribute the physical origins of the SIA to the structure-tunable competitions among interactions between the t_{2g} and e_g orbitals on the Fe³⁺ site through SOC effects. This effect leads to an easy plane perpendicular to x, y, and z through $|x^2-y^2\uparrow\rangle/|z^2\uparrow\rangle$ and $|yz\downarrow\rangle$, $|x^2-y^2\uparrow\rangle/|z^2\uparrow\rangle$ and $|xz\downarrow\rangle$, and $|x^2-y^2\uparrow\rangle$ and $|xy\downarrow\rangle$ interactions, respectively.

E. Tunable magnetic anisotropy in AA′BB′O₆ double perovskites

Although we predict the ferroelectric control of the magnetic anisotropy in HIF (ABO₃)₁/(A′BO₃)₁ superlattices with BiFeO₃/LaFeO₃ as a representative compound, the magnetic state is usually antiferromagnetic (G-type spin order in BiFeO₃/LaFeO₃), despite weak ferromagnetism arising from the DM interactions [i.e., the second term in Eq. (1)]. Here, we are more interested in applying the above mechanism to ferromagnetic or ferrimagnetic materials, which is technologically preferable. We next examine the recently proposed HIF AA′BB′O₆ double perovskites [60], i.e., LaRNiMnO₆ (R is the rare-earth ion), in which both ferroelectricity in the polar-chiral $P2_1$ structure and strong ferromagnetism (1.54 μ_B for Ni²⁺ and 3.13 μ_B for Mn⁴⁺ [60]) were predicted but without apparent strong magnetoelectric coupling. We first confirm that the P to NP transition occurs in HIF AA′BB′O₆ double perovskites, using LaYNiMnO₆ as an experimentally accessible member of the LaRNiMnO₆ (R is the rare-earth ion) family by considering that the Bi₂NiMnO₆/La₂NiMnO₆ superlattices were experimentally synthesized [61]. Figure 1(c) shows that the polar to nonpolar ($P2_1$ to $P\bar{1}$) transition occurs at ≈0% strain along with a sudden change of the polarization from 9 μC/cm² to zero. We next investigate whether the structure- and orbital-based magnetocrystalline anisotropy theory previously described for HIF (ABO₃)₁/(A′BO₃)₁ superlattices also applies to HIF AA′BB′O₆ double perovskites.

Our DFT+U+SOC calculations on LaYNiMnO₆ show that the magnetic anisotropy in polar $P2_1$ with FM spin order is along the out of plane direction, whereas it switches to be mostly in the (1$\bar{1}$0) plane with a 50% decrease in the out of plane component in $P\bar{1}$. The SIA model also reveals a large difference in the magnetic anisotropy between the two phases as displayed in Fig. 1(d), although the magnetic anisotropy slightly deviates away from the out of plane direction

predicted by the SIA model in $P2_1$ compared with our direct DFT calculations. Our symmetry-mode analysis of the SIA shows [53], as in the ferrate superlattice, that the in-phase and out of phase OOR modes exert the same effect on the SIA. In addition, the OOT mode dominates the OOR contribution in determining the SIA direction. The magnetic anisotropy in the nonpolar $P\bar{1}$ phase is ultimately determined by further including the AFE modes induced by the OOT modes. Therefore, the decoupling of the OOT modes also results in the different SIA on the magnetic ions, thus leading to very different magnetic anisotropies between the two $AA'BB'O_6$ double perovskite phases.

Next, we assess whether it is the same physical orbital interactions as in the HIF $(ABO_3)_1/(A'BO_3)_1$ superlattices that permit the change of the magnetic anisotropy across the P to NP transition. First, we identify the orbital configurations of Mn^{4+} and Ni^{2+} in $LaYNiMnO_6$ from Figs. 4(b) and 4(c) (see also the Supplemental Material Ref. [53]). In the polar $P2_1$ and $P\bar{1}$ phases, we find $(|xy\uparrow\rangle, |xz\uparrow\rangle, |yz\uparrow\rangle)^1 < (|x^2 - y^2\uparrow\rangle, |z^2\uparrow\rangle)^0 < (|xy\downarrow\rangle, |xz\downarrow\rangle, |yz\downarrow\rangle)^0 < (|x^2 - y^2\downarrow\rangle, |z^2\downarrow\rangle)^0$ and $(|xy\uparrow\rangle, |xz\uparrow\rangle, |yz\uparrow\rangle)^1 \approx (|xy\downarrow\rangle, |xz\downarrow\rangle, |yz\downarrow\rangle)^1 < (|x^2 - y^2\uparrow\rangle, |z^2\uparrow\rangle)^1 < (|x^2 - y^2\downarrow\rangle, |z^2\downarrow\rangle)^0$ for Mn^{4+} and Ni^{2+} ions, respectively. It should be noted that neither the xy, xz, yz orbitals in either the spin up or spin down manifolds are degenerate nor are the $|x^2 - y^2\rangle, |z^2\rangle$ orbitals. From perturbation theory, we find that the SOC interactions will mix $(|xy\uparrow\rangle, |xz\uparrow\rangle, |yz\uparrow\rangle)^1$ and $(|x^2 - y^2\uparrow\rangle, |z^2\uparrow\rangle)^0$ on Mn^{4+} and $(|xy\downarrow\rangle, |xz\downarrow\rangle, |yz\downarrow\rangle)^1$ and $(|x^2 - y^2\downarrow\rangle, |z^2\downarrow\rangle)^0$ on Ni^{2+} through the spin-conserving terms: $\hat{H}_{SO}^0 = \lambda \hat{S}_{z'}(\hat{L}_z \cos\theta + \frac{1}{2}\hat{L}_+ e^{-i\varphi}\sin\theta + \frac{1}{2}\hat{L}_- e^{i\varphi}\sin\theta)$. As can be seen in Table I, for Mn^{4+}, $|x^2 - y^2\uparrow\rangle$ can interact with $|xy\uparrow\rangle$ through $\hat{L}_z$, leading to out of plane SIA; $|x^2 - y^2\uparrow\rangle/|z^2\uparrow\rangle$ can interact with $|xz\uparrow\rangle$ through $\hat{L}_+/\hat{L}_-$, leading to in-plane SIA along the y direction; and $|x^2 - y^2\uparrow\rangle/|z^2\uparrow\rangle$ can interact with $|yz\uparrow\rangle$ through $\hat{L}_+/\hat{L}_-$, leading to in-plane SIA along the x direction. Because the energy levels of the $|x^2 - y^2\uparrow\rangle, |z^2\uparrow\rangle$ states and $|xy\uparrow\rangle$, $|xz\uparrow\rangle$, $|yz\uparrow\rangle$ states are nearly degenerate, the competitions among the interactions between $|x^2 - y^2\uparrow\rangle$ and $|xy\uparrow\rangle$ and between $|x^2 - y^2\uparrow\rangle/|z^2\uparrow\rangle$ and $|xz\uparrow\rangle/|yz\uparrow\rangle$ are highly susceptible to changes in the coordination geometry of the magnetic ions, which enables structure-based control over the orbital interactions and SIA. We deduce similar conclusions for Ni^{2+} between $(|xy\downarrow\rangle, |xz\downarrow\rangle, |yz\downarrow\rangle)^1$ and $(|x^2 - y^2\downarrow\rangle, |z^2\downarrow\rangle)^0$. Therefore, the structural tunable competitions among the interactions between the t_{2g} and e_g orbitals on the magnetic ions through SOC effects are also the origin of the ferroelectric control of the magnetic anisotropy in HIF $AA'BB'O_6$ double perovskites. The most striking phenomenon here is the ferroelectric control of strong out of plane ferromagnetism in $LaYNiMnO_6$ through the P to NP transition. Even with antiferromagnetic spin order in $AA'BB'O_6$ double perovskites, the ferroelectric control of large out of plane magnetization (i.e., ferrimagnetism) may also be realized by chemical selection of magnetic moments of the B and B' cations, such as in Ca_2FeOsO_6 and Ca_2FeMoO_6 compounds with G-type spin orders in the $P2_1/n$ structure [62,63]. This centrosymmetric $P2_1/n$ structure is a potential candidate for realizing the $P2_1$ polar structure in the $AA'BB'O_6$ chemistry if A-site substitution can achieve [001] layered cation

order, for example, in a thin film along the crystal growth direction [64,65].

We finally compute the energy barriers corresponding to viable transition paths between $Pmc2_1$ and $P2_1/m$ in $BiFeO_3/LaFeO_3$ and between $P2_1$ and $P\bar{1}$ in $LaYNiMnO_6$ [66]. We find that the energy barrier in $BiFeO_3/LaFeO_3$ can be as low as 77 meV/f.u. [53], which is much smaller than completely switching the polarization in $Pmc2_1$ to its opposite direction (136 meV/f.u.) [42]. There are two reasons for the low-energy barrier for the $Pmc2_1$ to $P2_1/m$ transition: first, we consider a "two-step" transition process. The polar to nonpolar transition is part of the polarization reversal process, which is energetically more favorable than a one-step process through a higher-energy intermediate [67,68]. Second, our nonpolar phase, which serves as the intermediate state for the polarization reversal [67,68], is also low in energy. The energy barrier is 242 meV/f.u in $LaYNiMnO_6$ [53]. A previous study indicated that the energy barrier can be reduced either by using compressive strain or by chemical substitution to achieve smaller OOR and OOT angles [42,69], which may be helpful for finding other compounds exhibiting ferroelectric control of strong out of plane ferromagnetism in $LaRNiMnO_6$ (R is the rare-earth ion) [60] near room temperature through the ferroelectric ($P2_1$) to antiferroelectric ($P\bar{1}$) phase transition.

III. POSSIBLE FERROELECTRIC CONTROL OF PERPENDICULAR MAGNETIC ANISOTROPY

Although there are many efforts at delivering ferroelectric control of the perpendicular magnetic anisotropy, these strategies are based on interfacial effects and leverage the strain generated by the substrate or changes of the electronic structures at the interfaces under an applied electric field [12–15,34,70]. Intrinsic ferroelectric control of the perpendicular magnetic anisotropy in multiferroics without strain mediation remains rare. Our study delivers microscopic insight into the application of recent magnetic anisotropy control by oxygen octahedral tilt in the field of ferroelectric control of the perpendicular magnetic anisotropy [71,72], where the out of plane magnetization can be changed in our studies, due to the changes of the magnetic anisotropy. Moreover, ferroelectric control of the perpendicular magnetic anisotropy offers advantages over electric control of the transition between antiferromagnetic and ferromagnetic spin orders [27–29]. The former case relies on the change of SIA energy, which is much weaker than changing the spin exchange interactions among the magnetic ions [see the first term in Eq. (1)] in the latter case. The lower magnetic transition barrier may facilitate the simultaneous change of the electric and magnetic signals in an application. Although there are other routes to control the magnetic anisotropy, such as strain effects [73], ion substitution [74], film reorientation [75], and varying thickness of the film with the changes of the oxygen octahedral tilt [71,72], they cannot be dynamically reversible.

Experimentally in thin films [12–15,34,73], consideration of shape anisotropy is another importance factor which usually leads to in-plane magnetic anisotropy in FM thin films, but disappears in bulk samples. The influence of this effect can be minimized or overcome by judicious choice of operating
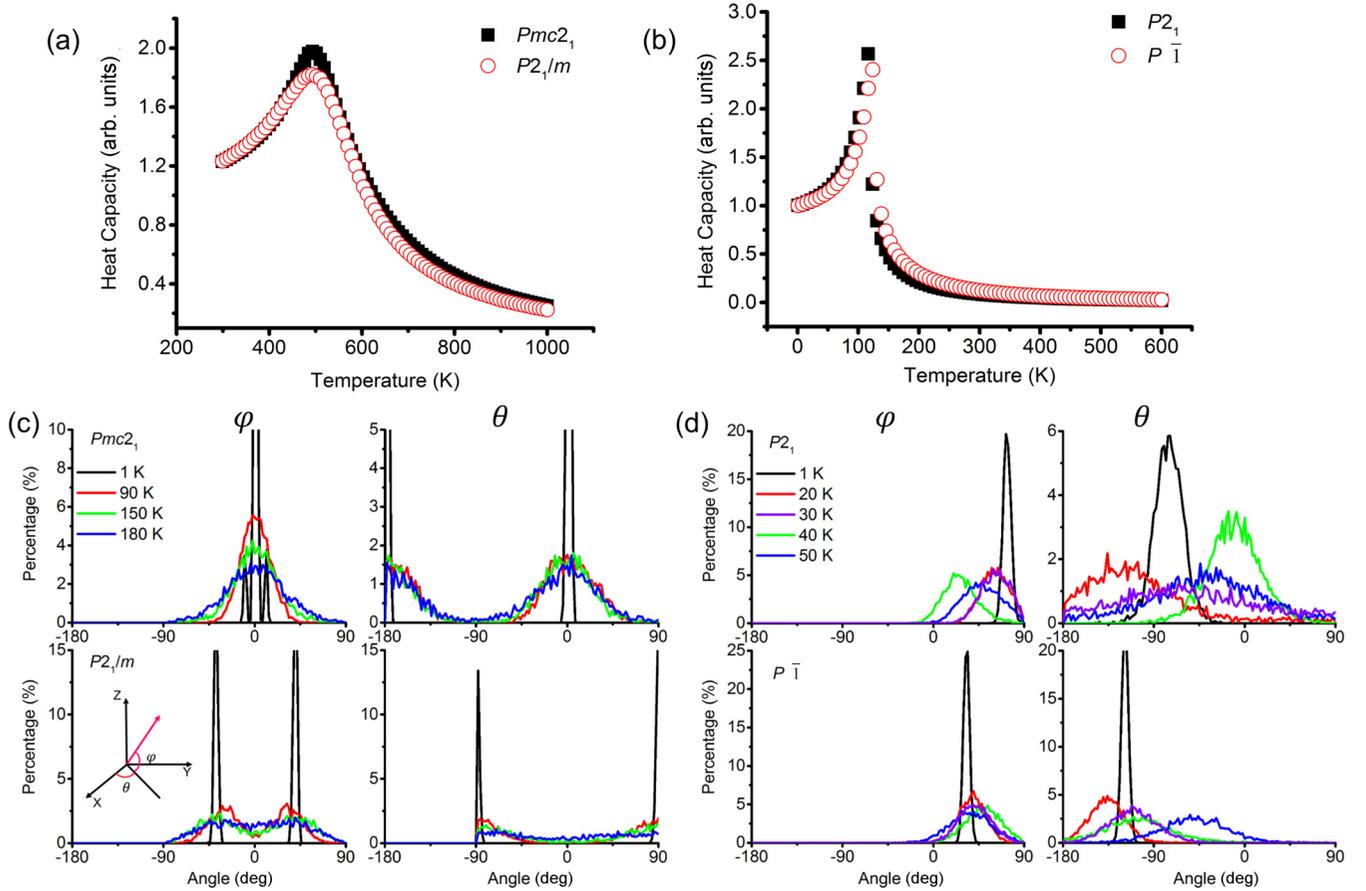
FIG. 5. Magnetic transition temperatures for (a) $BiFeO_3/LaFeO_3$ and (b) $LaYNiMnO_6$ and temperature dependencies of the magnetic anisotropies in (c) $BiFeO_3/LaFeO_3$ and (d) $LaYNiMnO_6$, which are obtained by carrying out Monte Carlo simulations [53,79]. Here, an $8 \times 12 \times 12$ supercell of the 20-atom unit cell in the $Pmc2_1$ and $P2_1$ phases was used and an $8 \times 8 \times 8$ supercell of the 40-atom unit cell in the $P2_1/m$ and $P\bar{1}$ phases was used in the Monte Carlo simulations. In the simulations, only symmetric spin exchange interactions in Eq. (1) were included for (a), (b). In (c), (d), we collected the spin directions in identically sized supercells, but both symmetric spin-exchange interactions and single-ion anisotropic terms in Eq. (1) were included. Percentage = (number of spin sites having the spin directions with the angles θ and φ)/(number of all spin sites). Angles θ and φ are defined in the coordinate system as shown. They correspond to the in-plane angle about the x direction and the out of plane angle about the in-plane projection of the spin, respectively. It should be noted that there are two peaks in $BiFeO_3/LaFeO_3$, because its magnetic structure is antiferromagnetic and comprises two magnetic sublattices.

temperature or strain [76–78]. If the magnetic anisotropy is strong as in Fe, Os, and Mo compounds [36,62,63,65], the effects of the shape anisotropy can be negligible. There are also magnetic domains and domain walls in thin films. Compared with the ferroelectric domain walls, there frequently exist common 180° and 90° magnetic domain walls, to which the magnetization will be sensitive. For example, the polarization can be significantly weakened in 180° domain wall structures and changes direction in 90° domain walls [18–26], which is also the case for the magnetization in the magnetic domain walls. Although the magnetic anisotropy can be switched through the P to NP transition, the macroscopic magnetization may be null in 180° domain walls structure. If the polar and magnetic domains can be coupled to each other, such as in the coupling between polar and antiferromagnetic domains in $BiFeO_3$ [22], then the 90° domain walls structure can be expected to realize switchable magnetic anisotropy macroscopically.

We further consider the effects of temperature on the changes of the magnetic anisotropy across the phase transi-

tion. As shown in Figs. 5(a) and 5(b), the Néel temperature in $BiFeO_3/LaFeO_3$ is around 500 K and the Curie temperature in $LaYNiMnO_6$ is around 116 K at 0% strain. In $BiFeO_3/LaFeO_3$ the magnetic anisotropy in the $Pmc2_1$ phase is in plane along the x direction approaching 0 K, while the spins point away from the in-plane direction in the $P2_1/m$ phase, oriented about 45° and in the yz plane [Fig. 5(c)]. These results are consistent with the results from the model analysis based on the coefficients obtained from our DFT calculations. These differences in the magnetic anisotropies between the polar and nonpolar phases remain discernible up to 150 K, where we find that most of the spins still lie in plane in the polar phase and many spins in the nonpolar phase are oriented 45° away from the in-plane orientation and close to the yz plane. We also find that the width of the peak, indicating the out of plane spin direction (φ), becomes broader at higher temperature, which indicates that thermal effects effectively reduce the magnetic anisotropy term in the spin Hamiltonian. As a result, the spin orientations are more broadly distributed.
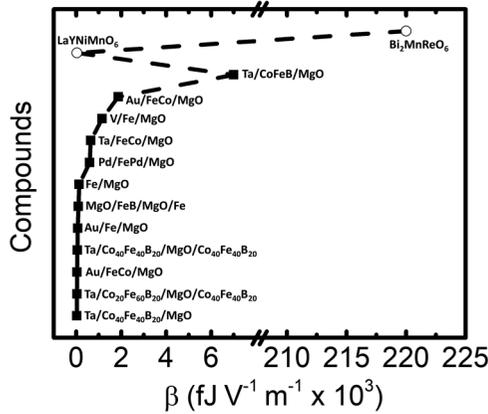
FIG. 6. VCMA coefficient β in MTJ and multiferroic heterostructures. The opened circle represents the result from our work. $\beta = \frac{\Delta MA}{\Delta E_I}$ where ΔMA is the change of the perpendicular magnetic anisotropy (i.e., the changes of the out of plane magnetization in our study) induced by the change of internal electric field ΔE_I. ΔE_I can be related to the external field (ΔE_{ext}) given the dielectric constant ε of the material: $\Delta E_I = \Delta E_{ext}/\varepsilon$. See the Supplemental Material [53] for references for reported β values.

In LaYNiMnO$_6$ upon approaching 0 K, the magnetic anisotropy in the $P2_1$ phase is close to the z axis (around 75°) and the yz plane. In contrast in the $P\bar{1}$ phase, the spins are oriented close to the in-plane direction around 30° and lie close to the y axis (around −120°). These temperature dependent anisotropies are consistent with the results from the model analysis with the coefficients obtained from our DFT calculations. This difference in the magnetic anisotropies between the polar and nonpolar phases remains discernible up to 40 K. We can also see that the position of magnetic anisotropy varies more widely at higher temperature in LaYNiMnO$_6$. For example, at 40 K the magnetic anisotropy in the polar phase approaches the in-plane direction and spins aligned along the in-plane spin direction tend towards the x direction, which is opposite to the behavior observed at lower temperatures. In contrast, the spin alignment in BiFeO$_3$/LaFeO$_3$ evolves smoothly with temperature. The reason for the stronger temperature dependent loss in spin orientational preferences in LaYNiMnO$_6$ may be attributed to its weaker magnetic anisotropy compared to BiFeO$_3$/LaFeO$_3$.

Our study also provides an alternative route to find materials with large voltage control of magnetic anisotropy (VCMA) coefficient (Fig. 6 and Refs. [53,80–82]). The VCMA coefficient in single component multiferroics, resulting from the ferroic phase transition induced changes in the perpendicular magnetic anisotropy (i.e., the out of plane magnetization in our case), can be as large as $\sim 10^5$ in Bi$_2$MnReO$_6$. Thus,

we show in theory that the VCMA coefficient in Bi$_2$MnReO$_6$ can be two orders larger than those found in magnetic tunnel junctions (MTJs), which indicates strong modulation of H_r (resonance field) and H_c (magnetic coercive field) under an applied electric field. Even in LaYNiMnO$_6$ with its weak magnetic anisotropy, we predict the VCMA coefficient can be comparable to the VCMA coefficients in MTJs (Fig. 6).

IV. CONCLUSIONS

Our theory is neither limited to the compounds presented in this work nor limited to HIF materials (see Table II), because the basic approach for the magnetic anisotropy control is based on two principles: First, how the d orbitals split under an octahedral field—selecting magnetic ions in the compound having d-orbital configurations with the highest occupied or lowest unoccupied orbitals including a xy orbital nearly degenerate with at least one of the other two t_{2g} orbitals. For example, this criterion is satisfied by choosing ions with d^3, d^5, or d^8 electron fillings on at least one magnetic octahedral site in the crystal. Note that our theory does not apply to magnetic ions with orbital degeneracies such that the highest occupied orbital is degenerate with the lowest unoccupied orbital so as to yield a first order Jahn-Teller instability [52,59]. The Jahn-Teller distortion would lift the degeneracy and result in a dominate SOC interaction between the highest occupied orbital degenerate with the lowest unoccupied orbital. In this case, the SIA is solely determined by this SOC interaction and there are no competing (comparable in energy) interactions available for modulation. The next principle is a polymorphism criterion: ferroelectric-ferroelectric or ferroelectric-antiferroelectric phase competitions between two structures having significantly different magnetic ion coordination environments. Examples of transitions involving these changes in the BO$_6$ octahedral geometry include HIF with changes in the OOT pattern and competitive ferroic phases in thin films with different symmetries. The transitions between the two states involved in the polymorphism can be realized by carefully investigating potential metastable structures and assessing their different coupling to an electric field through a $\boldsymbol{P} \cdot \boldsymbol{E}$ term [83,84]. Our theory is quite flexible in realization and may pave a way to find the ideal multiferroics for the application of so called four-state memory devices [9].

TABLE II. Compounds identified fulfilling the proposed orbital configuration and ferroic transition criteria to achieve changes in magnetic anisotropy (MA).

Compounds	d Orbital configuration	Magnetism	Ferroic transition	MA changes
BiFeO$_3$/LaFeO$_3$	d^5	Weak FM	$Pmc2_1$ to $P2_1/m$	[1$\bar{1}$0] to [011]
LaYNiMnO$_6$	d^3 and d^8	FM	$P2_1$ to $P\bar{1}$	[001] to [−0.44, −0.73,0.52]
Bi$_2$MnReO$_6$	d^3 and d^8	Ferrimagnetism	$R3$ to $P2/n$	[0.49,0.64,0.60] to [001]

[1] S. Manipatruni, D. E. Nikonov, C.-C. Lin, T. A. Gosavi, H. Liu, B. Prasad, Y.-L. Huang, E. Bonturim, R. Ramesh, and I. A. Young, Nature **565**, 35 (2019).

[2] S. Fusil, V. Garcia, A. Barthelemy, and M. Bibes, Annu. Rev. Mater. Res. **44**, 91 (2014).

[3] D. Chiba, M. Yamanouchi, F. Matsukura, and H. Ohno, Science **301**, 943 (2003).

[4] M. Weisheit, S. Fähler, A. Marty, Y. Souche, C. Poinsignon, and D. Givord, Science **315**, 349 (2007).

[5] D. Chiba, M. Sawicki, Y. Nishitani, Y. Nakatani, F. Matsukura, and H. Ohno, Nature **455**, 515 (2008).

[6] I. Stolichnov, S. W. E. Riester, H. J. Trodahl, N. Setter, A. W. Rushforth, K. W. Edmonds, R. P. Campion, C. T. Foxon, B. L. Gallagher, and T. Jungwirth, Nat. Mater. **7**, 464 (2008).

[7] S.-W. Cheong and M. Mostovoy, Nat. Mater. **6**, 13 (2007).

[8] R. Ramesh and N. A. Spaldin, Nat. Mater. **6**, 21 (2007).

[9] M. Fiebig, T. Lottermoser, D. Meier, and M. Trassin, Nat. Rev. Mater. **1**, 16046 (2016).

[10] C.-G. Duan, S. S. Jaswal, and E. Y. Tsymbal, Phys. Rev. Lett. **97**, 047201 (2006).

[11] J. M. Rondinelli, M. Stengel, and N. A. Spaldin, Nat. Nanotechnol. **3**, 46 (2008).

[12] T. Maruyama, Y. Shiota, T. Nozaki, K. Ohta, N. Toda, M. Mizuguchi, A. A. Tulapurkar, T. Shinjo, M. Shiraishi, S. Mizukami, Y. Ando, and Y. Suzuki, Nat. Nanotechnol. **4**, 158 (2009).

[13] W.-G. Wang, M. Li, S. Hageman, and C. L. Chien, Nat. Mater. **11**, 64 (2012).

[14] Y. Shiota, T. Nozaki, F. Bonell, S. Murakami, T. Shinjo, and Y. Suzuki, Nat. Mater. **11**, 39 (2012).

[15] X. He, Y. Wang, N. Wu, A. N. Caruso, E. Vescovo, K. D. Belashchenko, P. A. Dowben, and C. Binek, Nat. Mater. **9**, 579 (2010).

[16] G. Radaelli, D. Petti, E. Plekhanov, I. Fina, P. Torelli, B. R. Salles, M. Cantoni, C. Rinaldi, D. Gutiérrez, G. Panaccione, M. Varela, S. Picozzi, J. Fontcuberta, and R. Bertacco, Nat. Commun. **5**, 3404 (2014).

[17] J. A. Mundy, C. M. Brooks, M. E. Holtz, J. A. Moyer, H. Das, A. F. Rébola, J. T. Heron, J. D. Clarkson, S. M. Disseler, Z. Liu et al., Nature **537**, 523 (2016).

[18] J. Wang, J. B. Neaton, H. Zheng, V. Nagarajan, S. B. Ogale, B. Liu, D. Viehland, V. Vaithyanathan, D. G. Schlom, U. V. Waghmare, N. A. Spaldin, K. M. Rabe, M. Wuttig, and R. Ramesh, Science **299**, 1719 (2003).

[19] T. Zhao, A. Scholl, F. Zavaliche, K. Lee, M. Barry, A. Doran, M. P. Cruz, Y. H. Chu, C. Ederer, N. A. Spaldin, R. R. Das, D. M. Kim, S. H. Baek, C. B. Eom, and R. Ramesh, Nat. Mater. **5**, 823 (2006).

[20] Y.-H. Chu, L. W. Martin, M. B. Holcomb, M. Gajek, S.-J. Han, Q. He, N. Balke, C.-H. Yang, D. Lee, W. Hu, Q. Zhan, P.-L. Yang, A. Fraile-Rodriguez, A. Scholl, S. X. Wang, and R. Ramesh, Nat. Mater. **7**, 478 (2008).

[21] T. Choi, Y. Horibe, H. T. Yi, Y. J. Choi, W. Wu, and S.-W. Cheong, Nat. Mater. **9**, 253 (2010).

[22] J. T. Heron, M. Trassin, K. Ashraf, M. Gajek, Q. He, S. Y. Yang, D. E. Nikonov, Y.-H. Chu, S. Salahuddin, and R. Ramesh, Phys. Rev. Lett. **107**, 217202 (2011).

[23] B. B. Van Aken, T. T. M. Palstra, A. Filippetti, and N. A. Spaldin, Nat. Mater. **3**, 164 (2004).

[24] Y. Kumagai and N. Spaldin, Nat. Commun. **4**, 1540 (2013).

[25] S. Artyukhin, K. T. Delaney, N. A. Spaldin, and M. Mostovoy, Nat. Mater. **13**, 42 (2014).

[26] H. Das, A. L. Wysocki, Y. Geng, W. Wu, and C. J. Fennie, Nat. Commun. **5**, 2998 (2014).

[27] C. J. Fennie and K. M. Rabe, Phys. Rev. Lett. **97**, 267602 (2006).

[28] J. H. Lee, L. Fang, E. Vlahos, X. Ke, Y. W. Jung, L. F. Kourkoutis, J.-W. Kim, P. J. Ryan, T. Heeg, M. Roeckerath et al., Nature **466**, 954 (2010).

[29] J. H. Lee and K. M. Rabe, Phys. Rev. Lett. **104**, 207204 (2010).

[30] E. Bousquet, M. Dawber, N. Stucki, C. Lichtensteiger, P. Hermet, S. Gariglio, J.-M. Triscone, and P. Ghosez, Nature **452**, 732 (2008).

[31] N. A. Benedek and C. J. Fennie, Phys. Rev. Lett. **106**, 107204 (2011).

[32] A. B. Harris, Phys. Rev. B **84**, 064116 (2011).

[33] J. M. Rondinelli and C. J. Fennie, Adv. Mater. **24**, 1961 (2012).

[34] S. Ikeda, K. Miura, H. Yamamoto, K. Mizunuma, H. D. Gan, M. Endo, S. Kanai, J. Hayakawa, F. Matsukura, and H. Ohno, Nat. Mater. **9**, 721 (2010).

[35] A. Hirohata, W. Frost, M. Samiepour, and J.-Y. Kim, Materials **11**, 105 (2018).

[36] P. S. Wang, W. Ren, L. Bellaiche, and H. J. Xiang, Phys. Rev. Lett. **114**, 147204 (2015).

[37] J. Feng, K. Xu, L. Bellaiche, and H. J. Xiang, New J. Phys. **20**, 053025 (2018).

[38] Y. S. Oh, X. Luo, F.-T. Huang, Y. Wang, and S.-W. Cheong, Nat. Mater. **14**, 407 (2015).

[39] M. S. Senn, A. Bombardi, C. A. Murray, C. Vecchini, A. Scherillo, X. Luo, and S. W. Cheong, Phys. Rev. Lett. **114**, 035701 (2015).

[40] X. Q. Liu, J. W. Wu, X. X. Shi, H. J. Zhao, H. Y. Zhou, R. H. Qiu, W. Q. Zhang, and X. M. Chen, Appl. Phys. Lett. **106**, 202903 (2015).

[41] M. H. Lee, C.-P. Chang, F.-T. Huang, G. Y. Guo, B. Gao, C. H. Chen, S.-W. Cheong, and M.-W. Chu, Phys. Rev. Lett. **119**, 157601 (2017).

[42] Z. Zanolli, J. C. Wojdeł, J. Íñiguez, and P. Ghosez, Phys. Rev. B **88**, 060102(R) (2013).

[43] X.-Z. Lu and J. M. Rondinelli, Nat. Mater. **15**, 951 (2016).

[44] X.-Z. Lu and J. M. Rondinelli, Adv. Funct. Mater. **27**, 1604312 (2017).

[45] J. P. Perdew, A. Ruzsinszky, G. I. Csonka, O. A. Vydrov, G. E. Scuseria, L. A. Constantin, X. Zhou, and K. Burke, Phys. Rev. Lett. **100**, 136406 (2008).

[46] G. Kresse and J. Furthmüller, Phys. Rev. B **54**, 11169 (1996).

[47] G. Kresse and J. Furthmüller, Comput. Mater. Sci. **6**, 15 (1996).

[48] G. Kresse and D. Joubert, Phys. Rev. B **59**, 1758 (1999).

[49] X.-Z. Lu and J. M. Rondinelli, Phys. Rev. Mater. **2**, 054409 (2018).

[50] X. Z. Lu, X. G. Gong, and H. J. Xiang, Comput. Mater. Sci. **91**, 310 (2014).

[51] H. J. Xiang, E. J. Kan, S.-H. Wei, M.-H. Whangbo, and X. G. Gong, Phys. Rev. B **84**, 224429 (2011).

[52] H. Xiang, C. Lee, H.-J. Koo, X. Gong, and M.-H. Whangbo, Dalton Trans. **42**, 823 (2013).

[53] See Supplemental Material at http://link.aps.org/supplemental/10.1103/PhysRevB.103.184417 for computational methods, reliability of the PBEsol functional, steps to compute the magnetic anisotropy for the unit cell, SIA coefficients for the polar and nonpolar structures in $BiFeO_3/LaFeO_3$ and $LaYNiMnO_6$ compounds, strain effects on the magnetic anisotropy, effects of the DM-exchange interaction on the magnetic anisotropy in the $P2_1$ and $P\bar{1}$ phases, density of states (DOS) and U and SOC effects, phonon modes and effects of each mode on the SIA in the $P2_1$ and $P\bar{1}$ phases of $LaYNiMnO_6$, energy barriers between the $Pmc2_1$ and $P2_1/m$ phases at 0% strain of $BiFeO_3/LaFeO_3$ and between the $P2_1$ and P1 phases at 0% strain of $LaYNiMnO_6$, the theory applied to the $R3$ and $P2_1/n$ phases Bi_2MnReO_6, and the VCMA coefficients in $LaYNiMnO_6$ and Bi_2MnReO_6.

[54] T. Moriya, Phys. Rev. **120**, 91 (1960).

[55] T. Moriya, Phys. Rev. Lett. **4**, 228 (1960).

[56] M. Matsuda, R. S. Fishman, T. Hong, C. H. Lee, T. Ushiyama, Y. Yanagisawa, Y. Tomioka, and T. Ito, Phys. Rev. Lett. **109**, 067205 (2012).

[57] C. Weingart, N. Spaldin, and E. Bousquet, Phys. Rev. B **86**, 094413 (2012).

[58] X. Ke, T. Birol, R. Misra, J.-H. Lee, B. J. Kirby, D. G. Schlom, C. J. Fennie, and J. W. Freeland, Phys. Rev. B **88**, 094434 (2013).

[59] M.-H. Whangbo, E. E. Gordon, H. Xiang, H.-J. Koo, and C. Lee, Acc. Chem. Res. **48**, 3080 (2015).

[60] H. J. Zhao, W. Ren, Y. Yang, J. Íñiguez, X. M. Chen, and L. Bellaiche, Nat. Commun. **5**, 4021 (2014).

[61] P. Padhan, P. LeClair, A. Gupta, M. A. Subramanian, and G. Srinivasan, J. Phys.: Condens. Matter **21**, 306004 (2009).

[62] C. Ritter, M. R. Ibarra, L. Morellon, J. Blasco, J. García, and J. M. De Teresa, J. Phys.: Condens. Matter **12**, 8295 (2000).

[63] H. L. Feng, M. Arai, Y. Matsushita, Y. Tsujimoto, Y. Guo, C. I. Sathish, X. Wang, Y.-H. Yuan, M. Tanaka, and K. Yamaura, J. Am. Chem. Soc. **136**, 3326 (2014).

[64] G. King and P. M. Woodward, J. Mater. Chem. **20**, 5785 (2010).

[65] M. Ležaić and N. A. Spaldin, Phys. Rev. B **83**, 024410 (2011).

[66] G. Henkelman, B. P. Uberuaga, and H. A. Jónsson, J. Chem. Phys. **113**, 9901 (2000).

[67] J. T. Heron, J. L. Bosse, Q. He, Y. Gao, M. Trassin, L. Ye, J. D. Clarkson, C. Wang, J. Liu, S. Salahuddin, D. C. Ralph, D. G. Schlom, J. Íñiguez, B. D. Huey, and R. Ramesh, Nature **516**, 370 (2014).

[68] E. A. Nowadnick and C. J. Fennie, Phys. Rev. B **94**, 104105 (2016).

[69] A. T. Mulder, N. A. Benedek, J. M. Rondinelli, and C. J. Fennie, Adv. Func. Mater. **23**, 4810 (2013).

[70] Q. Yang, T. Nan, Y. Zhang, Z. Zhou, B. Peng, W. Ren, Z.-G. Ye, N. X. Sun, and M. Liu, Phys. Rev. Appl. **8**, 044006 (2017).

[71] Z. Liao, M. Huijben, Z. Zhong, N. Gauquelin, S. Macke, R. J. Green, S. Van Aert, J. Verbeeck, G. Van Tendeloo, K. Held, G. A. Sawatzky, G. Koster, and G. Rijnders, Nat. Mater. **15**, 425 (2016).

[72] D. Kan, R. Aso, R. Sato, M. Haruta, H. Kurata, and Y. Shimakawa, Nat. Mater. **15**, 432 (2016).

[73] C. Du, R. Adur, H. Wang, A. J. Hauser, F. Yang, and P. C. Hammel, Phys. Rev. Lett. **110**, 147204 (2013).

[74] D. Y. Charles, L. Flint, P. P. Balakrishnan, K. Mahalingam, B. Urwin, A. Vailionis, A. T. N'Diaye, P. Shafer, E. Arenholz, Y. Choi, K. H. Stone, J.-H. Chu, B. M. Howe, J. Liu, I. R. Fisher, and Y. Suzuki, Phys. Rev. Lett. **119**, 077201 (2017).

[75] J. H. Lee, K. T. Delaney, E. Bousquet, N. A. Spaldin, and K. M. Rabe, Phys. Rev. B **88**, 174426 (2013).

[76] G. Bayreuther, M. Dumm, B. Uhl, R. Meier, and W. Kipferl, J. Appl. Phys. **93**, 8230 (2003).

[77] M. Belmeguenai, S. Mercone, C. Adamo, L. Méchin, C. Fur, P. Monod, P. Moch, and D. G. Schlom, Phys. Rev. B **81**, 054410 (2010).

[78] G. Shibata, M. Kitamura, M. Minohara, K. Yoshimatsu, T. Kadono, K. Ishigami, T. Harano, Y. Takahashi, S. Sakamoto, Y. Nonaka *et al.*, npj Quantum Mater. **3**, 3 (2018).

[79] K. Hukushima and K. Nemoto, J. Phys. Soc. Jpn. **65**, 1604 (1996).

[80] K. L.Wang, J. G. Alzate, and P. Khalili Amiri, J. Phys. D: Appl. Phys. **46**, 074003 (2013).

[81] M. Liu and N. X. Sun, Philos. Trans. R. Soc. A **372**, 20120439 (2014).

[82] P. V. Ong, N. Kioussis, D. Odkhuu, P. Khalili Amiri, K. L. Wang, and G. P. Carman, Phys. Rev. B **92**, 020407(R) (2015).

[83] K. M. Rabe, in *Functional Metal Oxides: New Science and Novel Applications*, edited by S. Ogale, and V. Venkateshan (Wiley, New York, 2013).

[84] J. W. Bennett, K. F. Garrity, K. M. Rabe, and D. Vanderbilt, Phys. Rev. Lett. **110**, 017603 (2013).